Space Weather

RESEARCH ARTICLE
10.1029/2024SW004228

Quantitative Assessment of GOES 8–15 >0.6 and >4 MeV Radiation Belt Electron Fluxes

J. V. Rodriguez[1,2], **M. H. Denton**[3], **and A. Boudouridis**[1,2]

[1]Cooperative Institute for Research in Environmental Sciences, University of Colorado Boulder, Boulder, CO, USA, [2]National Centers for Environmental Information, NOAA, Boulder, CO, USA, [3]Center for Space Plasma Physics, Space Science Institute, Boulder, CO, USA

Key Points:

- The Geostationary Operational Environmental Satellites (GOES) 13–15 characterizations of the >0.6 and >4 MeV electron channels were more accurate than the GOES 8–12 characterizations
- The GOES 13–15 characterization of the >0.6 MeV channel and a new, more accurate characterization of the >4 MeV channel should be used
- The GOES-15 >0.6 and >4 MeV fluxes are lower than the GOES-17 fluxes in the same energy ranges

Correspondence to:
J. V. Rodriguez,
juan.v.rodriguez@colorado.edu

Citation:
Rodriguez, J. V., Denton, M. H., & Boudouridis, A. (2025). Quantitative assessment of GOES 8–15 >0.6 and >4 MeV radiation belt electron fluxes. *Space Weather*, *23*, e2024SW004228. https://doi.org/10.1029/2024SW004228

Received 24 OCT 2024
Accepted 7 FEB 2025

Author Contributions:
Conceptualization: J. V. Rodriguez, M. H. Denton
Data curation: J. V. Rodriguez, A. Boudouridis
Formal analysis: J. V. Rodriguez, A. Boudouridis
Funding acquisition: M. H. Denton
Methodology: J. V. Rodriguez
Software: J. V. Rodriguez
Validation: J. V. Rodriguez
Writing – original draft: J. V. Rodriguez
Writing – review & editing: J. V. Rodriguez, M. H. Denton, A. Boudouridis

Abstract On Geostationary Operational Environmental Satellites (GOES) 8–15 (1996–2020), the Energetic Particle Sensor (EPS) included three integral electron channels, with nominal lower energies of 0.6 MeV (E1), 2 MeV (E2) and 4 MeV (E3). The >2 MeV channel has received more attention than the other two channels, because it is used by the NOAA Space Weather Prediction Center for its radiation belt real-time alerts, and because the characterizations of E1 and E3 were ambiguous, due in part to processing changes between GOES-12 and -13. This paper reports the first cross-calibration of EPS E1 and E3 with the new Magnetospheric Particle Sensor—High Energy (MPS-HI) (first flown on GOES-16). It is based on observations from 2019, when GOES-15 and -17 were separated by 0.6 hr local time on average. The channel response functions (cm^2 sr vs. energy) were used three ways: in a bowtie analysis using the method used for the GOES-17 calibrations; in forward-model analyses to predict rates for comparison with observations; and in a spectral inversion for comparison of differential energy spectra from the two instruments. The results show that the GOES 13–15 characterizations were more accurate than the GOES 8–12 characterizations, and the bowtie characterization of E3 is still more accurate, while the GOES 13–15 characterization of E1 should continue to be used. The EPS E1 bias with respect to MPS-HI is −69%. In the E3 energy range, the EPS fluxes are lower than MPS-HI, from a factor of 2 at 3 MeV to a factor of 5 at 4.4 MeV.

Plain Language Summary For nearly 25 years, NOAA flew an instrument on eight geostationary weather satellites that measured Van Allen Belt electron fluxes in three energy ranges above 600 thousand electron volts. At these energies, electrons penetrate inside satellites to directly damage electronics, or to deposit charge and eventually discharge near sensitive components, causing damage or interference. The middle energy range, above 2 million electron volts, has been studied extensively because it is used by NOAA for real-time alerts of elevated spacecraft charging hazard. The other two energy ranges have not been studied as much because their calibrations have been uncertain and were changed by NOAA starting in 2010. By comparing these data to fluxes from the higher-resolution replacement instrument when they were unusually close together on-orbit, we determine which of the calibrations are closest to the new data and describe how to correct the older data.

1. Introduction

The first observations of radiation belt electron fluxes in geosynchronous orbit were made by multiple experiments on the Applications Technology Satellite 1 (ATS-1), launched in 1966 (Lanzerotti et al., 1967; Lezniak et al., 1968; Paulikas et al., 1968). Together, these experiments observed 50 keV - >1.9 MeV electrons. They made the first observations of phenomena that are now well-known in geosynchronous orbit such as particle injections, drift echoes and the diurnal flux variation. Subsequently, radiation belt fluxes in geosynchronous were also measured on ATS-5 (launched 1969) (Chanteur et al., 1977) and ATS-6 (launched 1974) (Paulikas et al., 1975). Observations from ATS-5 and ATS-6 of >0.7, >1.55, and >3.9 MeV electron fluxes were used by Paulikas and Blake (1979) in their pioneering correlation of radiation belt fluxes with solar wind velocity. Starting in 1974, the Energetic Particle Sensors (EPS) on the Synchronous Meteorological Satellites and GOES included a single channel for the measurement of MeV radiation belt electrons, usually with a lower energy of 2 MeV, sometimes 1.2 MeV (Grubb, 1975; Vampola, 1987). Originally intended to directly measure the fluxes causing background noise in the solar X-ray sensor (Grubb, 1975), data from this channel were used to attribute certain satellite anomalies to internal charging by penetrating MeV electrons (Vampola, 1987; Wrenn et al., 2002; Wrenn & Smith, 1996). For GOES 8, the EPS was redesigned to reduce the effects of radiation damage on the >2 MeV

channel and to add two electron channels, with nominal lower energies of 0.6 MeV (E1) and 4 MeV (E3) (Onsager et al., 1996; Panametrics, 1988; Sellers & Hanser, 1996). This trio of integral channels was included in every EPS flown on GOES 8–15 (data processed from 01 January 1996 through 04 March 2020).

When introduced, the EPS E1 channel was expected to improve estimates of the electron energy spectrum for use in internal charging analyses (Wrenn & Smith, 1996). Depending on the effective shielding thickness, energies less than or greater than 2 MeV may be associated with a specific susceptibility to internal charging. However, the >2 MeV channel (E2) has overshadowed the E1 and E3 channels in practice, in part because of its use by the NOAA Space Weather Prediction Center (SWPC) for its radiation belt (internal charging) alerts. Owing to this operational importance, >2 MeV fluxes in geostationary orbit (GEO) have been studied extensively (Baker et al., 2019; Balikhin et al., 2016; Boudouridis et al., 2020; Gannon et al., 2012; Meredith et al., 2015; Onsager et al., 2004; O'Brien et al., 2001). Another reason for the relative neglect of the E1 channel, despite its large geometrical factor and insensitivity to solar proton contamination (Rodriguez, 2014b), has been confusion about its characteristics. This confusion originates in its slowly rising energy response, which makes its effective lower energy and associated geometrical factor ambiguous. When the processing system changed between the GOES 8–12 and 13–15 series, SWPC changed the effective lower energy and geometrical factor used to process E1 while maintaining the characterization of E2. While this change was intended to improve the accuracy of the E1 characterization, it has added to the confusion surrounding this channel. Like E1, EPS E3 also has a slowly-rising energy response. Between GOES-12 and -13, SWPC also changed the geometrical factor used for processing E3, though not the effective lower energy. Unlike E1, E3 is sensitive to >38 MeV protons (Panametrics, 1995), resulting in high background levels (from galactic cosmic rays (GCRs) and solar energetic particles) compared to the electron fluxes. The algorithm implemented to correct this contamination in real time did not perform reliably. These problems have made the E3 channel data difficult to use. Nonetheless, the ∼25-year time series from the >0.6 MeV (E1) and >4 MeV (E3) channels presents an opportunity for long-term analysis of the dynamics of MeV electrons and their contributions to dose damage and internal charging in geostationary orbit. In order for the E1 and E3 fluxes to be used quantitatively, our understanding of their performance needs to be improved through an evaluation of their energy response functions and through cross-calibrations with higher-energy-resolution observations. This paper reports the results of the first such study of the GOES EPS E1 and E3 integral channels.

Starting with GOES-16, EPS has been replaced with the Space Environment In-Situ Suite (SEISS) (Dichter et al., 2015). The SEISS instrument that measures radiation belt fluxes is the Magnetospheric Particle Sensor - High Energy (MPS-HI). In addition to a >2 MeV channel for operational continuity, MPS-HI measures differential fluxes throughout the EPS energy range. The purpose of this paper is to report the first cross-calibration of the EPS E1 and E3 channels with MPS-HI and to determine the most accurate scalar geometric factors and effective lower energies for the calibration of these channels. Prior to this work, only EPS E2 had been cross-calibrated with MPS-HI, using different satellite pairs (Boudouridis et al., 2020). A period of nearly 16 months (12 November 2018–04 March 2020) when GOES-17 operated closer than usual to GOES-15 is used here for cross-calibration of the instruments on these two satellites. Past comparisons of GOES 8–15 EPS electron (E2) and proton (P1-P7) channels have demonstrated that the EPS design achieved good repeatability, with differences of 1%–30% (Meredith et al., 2015; Rodriguez, 2015; Rodriguez et al., 2014). In the light of this repeatability, with the same EPS design on GOES 8–15, the conclusions of this paper about the relative accuracies of the different historical calibrations of EPS channels E1 and E3 should apply to the entire GOES 8–15 EPS series.

Several steps are required to cross-calibrate EPS E1 and E3 with MPS-HI. Galactic cosmic ray backgrounds are removed from the highest energy electron channels prior to comparisons. The two laboratory calibrations of the EPS E1 response functions are evaluated critically to derive four versions of the response functions for use in a sensitivity study. These four versions are used in a forward-model calculation to predict E1 count rates from the MPS-HI differential flux spectrum for comparison with observed E1 rates. The bowtie analysis used for MPS-HI (Boudouridis et al., 2020) is used to derive new scalar geometric factors and effective energies for E1 and E3. These new characterizations are compared to those used by SWPC to process GOES 8–12 and GOES 13–15 data by using them to convert count rates to integral fluxes and comparing the results to MPS-HI spectra integrated above the effective energies. Differential electron spectra are inverted from the three EPS integral channels in order to compare the EPS and MPS-HI spectra above 3 MeV. Symmetric accuracy metrics (Morley et al., 2018) are used to quantify relative differences between different calibrations. We find that the GOES 13–15

characterization of E1 and E3 was successful in improving the accuracy of the reported fluxes; that the new bowtie characterizations are somewhat more accurate; and that there remain significant discrepancies between the EPS E1 and E3 fluxes and the MPS-HI fluxes, particularly above 3 MeV. Nonetheless, the cross-calibrations demonstrate that the EPS E1 fluxes are reliable over their entire dynamic range, despite large count rates at the highest flux levels. This fact is used to reliably bound the natural variability of the ratio of the >2 MeV to the >0.68 MeV electron fluxes in GEO during the study period.

2. Data and Study Period

The data used in this paper are from GOES-15 EPS and GOES-17 MPS-HI. We focus on 2019, when GOES-15 and GOES-17 were separated by 9.0° (0.6 hr local time) on average, which is closer than the usual 15-degree separation during on-orbit test (Boudouridis et al., 2020). At these longitudes (128–137° W), satellites in geostationary equatorial orbit are only ∼4 degrees north of the geomagnetic equator (Onsager et al., 2004).

GOES 13, 14 and 15 each flew two EPS units, one looking westward and one looking eastward. (On GOES 13–15, the original EPS sensor was renamed Energetic Proton, Electron and Alpha Detector (EPEAD). The design of the detector subsystems was the same, however. Unless a distinction needs to be drawn between the two series, we refer to the instrument as EPS throughout this paper.) Each EPS unit comprised one solid state telescope and three dome detectors (Sellers & Hanser, 1996). Under each dome, two 25 mm^2 area, 1500 μm thick surface barrier detectors were joined to create a single equivalent detector. The detector 3 (D3) dome reported the E1 (>0.6 MeV) and E2 (>2 MeV) channels, a solar energetic proton and a solar energetic alpha particle channel (Onsager et al., 1996). The detector 4 (D4) dome reported the E3 (>4 MeV) channel, a solar energetic proton and a solar energetic alpha particle channel (Onsager et al., 1996). Because the channels were discriminated solely by energy deposition in the detectors, the E2 and E3 electron channels were susceptible to proton contamination and could be dominated by proton fluxes during SEP events unless the electron fluxes were highly elevated.

The difference between the minimum and maximum pitch angles encompassed by the large EPS FOVs was 90–100°, with a central pitch angle near 90°, depending on the local orientation of the magnetic field. The EPS observations thus approximated an isotropic average of the integral directional number flux. In the present work, the EPS fluxes are treated as isotropic averages of integral differential flux (electrons/cm^2-sr-s). The EPS E1 and E2 data are from the "science-quality" reprocessed product (Rodriguez, 2014b). This product includes the application of a non-paralyzable dead time correction (Hanser, 2011; Meredith et al., 2015), which is dominated by the E1 count rates (Rodriguez, 2014b). We have avoided using electron fluxes from the GOES-15 EPEAD "W" sensor because it exhibited degradation on-orbit that depended on local time and season (Baker et al., 2019), perhaps due to seasonal and diurnal temperature variations. Therefore, all of the GOES-15 integral electron channels used in this paper are from the EPEAD "E" sensor and are referred to as E1E, E2E and E3E.

MPS-HI consists of five electron solid-state telescopes and five proton solid-state telescopes and two dosimeters (Dichter et al., 2015). Each MPS-HI electron telescope is comprised of nine solid state detectors (six of which are combined into one effective thick detector), which enable separation of the electron spectrum from 50 keV to 4 MeV into 10 differential channels and to produce an integral >2 MeV channel (E11) (Dichter et al., 2015). The differential channels have effective energies between 0.07 and 2.89 MeV (Boudouridis et al., 2020). Each telescope reports an additional integral channel with an onset at 4 MeV (E10A) that is not processed in real time. For comparison with the EPS fluxes, GOES-17 MPS-HI spectra from the multiple telescopes are combined to create isotropic averages of the differential directional flux (electrons/cm^2-sr-s-keV) (Sillanpää et al., 2017) using pitch angles (Rodriguez, 2014a) calculated from the GOES-17 magnetometer data (Rich et al., 2024). Following background removal, residuals below 0.1 e/cm^2-sr-s-keV are treated as insignificant and replaced with fill values prior to calculation of isotropic fluxes.

The EPS D3 dome geometric factor (0.75 cm^2 sr) is much larger then the MPS-HI geometric factor (0.001–0.002 cm^2 sr, energy-dependent), and the EPS dead time (2.5×10^{-6} s) is greater than the MPS-HI electron telescope dead time (8.0×10^{-7} s). Therefore, for the same input fluxes, the EPS E1 and E2 fluxes have a much larger dead time correction than the MPS-HI fluxes.

3. Analysis Methods

3.1. Forward Model Calculation and Spectral Inversion

In a forward model calculation, predicted channel counts λ are calculated by convolving a differential flux energy spectrum $j(E)$ with the energy response function (geometric factor) of a channel $G(E)$:

$$\lambda = \delta t \int_0^\infty j(E)G(E)dE \quad (1)$$

where δt is the accumulation period of the channel. In a cross-calibration, $j(E)$ is estimated from the observations of the instrument with finer energy resolution. An energy exponential (EE) spectrum, which is a reasonable approximation to observed 0.6–4 MeV electron spectra in GEO (Figure 6), can be used to perform a linear interpolation or fit to $\log(j)$ versus energy, for finer sampling of $G(E)$ than is provided by the differential flux measurements. The predicted counts λ are compared with the observed counts y, thus eliminating the uncertainty introduced by assumptions used to calculate a scalar geometric factor for the modeled channel. As a test of the accuracy of a scalar geometric factor G and the associated effective lower energy E_l, the predicted counts are also converted to integral fluxes using G and compared to fluxes calculated by integrating the finer-resolution electron spectra above E_l. In both cases, the comparisons are quantified using accuracy metrics (Morley et al., 2018).

The forward model calculation may also be used in a more advanced comparison. For the cross-calibration of EPS E3, differential electron flux spectra are inverted from the three EPS integral flux measurements, using the method of O'Brien and Morley (2011), for comparison with an observed differential electron spectrum. This inversion method uses an iterative forward model approach (see the appendix in Peck et al. (2015) for a detailed description of this method as tailored to another instrument). The difference between the observed set of channel counts $\vec{y}$ (from E1, E2, and E3) and $\vec{\lambda}$ is evaluated using a penalty function derived from $\vec{\lambda}$ and $\vec{y}$ using a Poisson model for counting statistical error and a Gaussian model for calibration error. The penalty function is minimized iteratively using the Nelder-Mead simplex method (Nelder & Mead, 1965). The result is a weighted sum of energy-exponential (EE) and relativistic Maxwellian (RM) spectra in which the weights are functions of the penalty function. A key strength of this approach is that it does not use a scalar geometric factor approximation, which relies on the assumption of a spectral form (or a set of spectra; see Section 3.2). However, it can only be used when at least three channels are reporting valid fluxes above backgrounds, which is rarely the case for EPS E1, E2, and E3.

3.2. Bowtie Analysis

While electron channel responses in solid state telescopes can be peaked within the desired energy bandpasses, high-energy tails in the responses caused by scattering of electrons within the telescope and bremsstrahlung (Tuszewski et al., 2004) present a challenge to characterization of such channels as differential bands. To derive pairs of effective energies and geometric factors, the channel energy responses are analyzed using the "bowtie" method with a set of spectra observed by instruments with similar or higher energy resolution (Boudouridis et al., 2020). Bowtie analysis can be performed on a channel by treating it as a differential (Selesnick & Blake, 2000) or an integral channel (Fillius & McIlwain, 1974; Van Allen et al., 1974). The error bars resulting from the natural variability of the chosen set of spectra indicate whether a given channel is more accurately treated as a differential or an integral channel. The analysis reports the median G (for integral channels) or GdE (for differential channels) and the difference between the median and 5th and 95th percentiles as asymmetric error bars. It also reports an effective lower energy E_l for integral channels or an effective energy E_{diff} for differential channels. The values in the (E_l, G) or (E_{diff}, GdE) pairs must be used together. The strength of this approach is to permit rapid calculation of fluxes from count rates of individual channels, without any dependence on other channels, along with an estimate of the error due to natural variability. Please see Boudouridis et al. (2020) for more details. A comparison of GOES-16 MPS-HI fluxes calibrated in this way with data from the Korean space weather monitor particle detector (KSEM PD) on GEO-KOMPSAT-2A (GK2A), a different design, has shown good agreement (Oh et al., 2024).

3.3. Background Removal

Several of the electron channels used in this analysis have responses to high-energy protons that result in a continuous background due to GCRs, below which electron fluxes cannot be observed, and occasionally a large response to a SEP event that dominates the counts for hours to days. For quantitative cross-calibration of their electron responses, the proton backgrounds need to be omitted from the comparisons. The EPS E1 and E2 channels and the MPS-HI E9, E10 and E11 channels have their backgrounds removed as part of the real-time processing. However, the real-time EPS E3 background removal was not reliable, and the MPS-HI E10A channel was not processed in real time. Therefore, we have removed the E3 and E10A backgrounds using an adaptation of the method developed originally for the real-time removal of MPS-HI backgrounds.

The method relies on the recognition that the background count rates are distributed normally (as the high-rate limit of a Poisson distribution), and that this Gaussian distribution is at the low end of the overall distribution of count rates. The greater the fraction of time the channel reports background levels, the more prominent this distribution is. It is assumed that the peak of this probability density function (pdf) and the part below the peak are dominated by the GCR count rates, while above the peak they merge with the count rates from the electrons. Therefore, this method fits the cumulative distribution function (cdf) below the count rate at which the peak of the pdf occurs. For a Gaussian with a pdf $f(x)$ given by

$$f(x) = \frac{b}{\sigma\sqrt{2\pi}} \exp\left[-\frac{(x-\mu)^2}{2\sigma^2}\right] \tag{2}$$

the cdf $F(x)$ is given by an error function (erf) as follows:

$$F(x) = \frac{b}{2}\left[1 + \mathrm{erf}\left(\frac{x-\mu}{\sigma\sqrt{2}}\right)\right] \tag{3}$$

This equation is fit to a cdf accumulated over a long period (e.g., a 27-day solar rotation), and the mean μ and standard deviation σ are recorded. An example of the results of this method is shown in Figure 1. This method has been used to determine the backgrounds in the GOES-15 EPS E3E channel from January 2011 to March 2020 (Bartels rotations (BR) 2421–2545). The E3 channel is sensitive to >38 MeV protons, but its response to higher energy protons may not be known sufficiently well for accurate conversion of these backgrounds to proton fluxes (Hanser, 2011). The clear long-term variation, with a minimum around BR 2465 (solar maximum) and a maximum around BR 2542 (solar minimum), indicates that these backgrounds are dominated by GCR protons. It also confirms that the removed background needs to be time-dependent. The removed backgrounds were calculated by assigning the values of μ calculated in this manner to the centers of the (non-overlapping) BR periods and interpolating linearly between them in order to avoid jumps. If a shorter point spacing is desired, overlapping periods rather than shorter, contiguous periods should be used to ensure a sufficient number of background samples for the analysis.

3.4. Accuracy Metrics

The symmetric signed percentage bias (SSPB) and median symmetric accuracy (ζ) metrics (Morley et al., 2018) are used to evaluate the cross-calibrations. These metrics are appropriate for radiation belt fluxes (Botek et al., 2023; Glauert et al., 2021; Minow et al., 2024; Morley et al., 2018; Simms et al., 2023), which vary by orders of magnitude, since they penalize under- and overpredictions equally. Both metrics are based on the logarithm of the accuracy ratio Q = prediction/observable. $M(x_i)$ indicates the median of the set of quantities x_i.

$$SSPB = 100\ \mathrm{sgn}(M(\ln(Q_i)))\left(\exp(|M(\ln(Q_i))|) - 1\right) \tag{4}$$

$$\zeta = 100\ \left(\exp(M(|\ln(Q_i)|)) - 1\right) \tag{5}$$

An interpretation of these quantities is that half the prediction errors are less than a factor of $1 + \zeta/100$, while the median prediction error is an overestimate by SSPB% (Morley et al., 2018). For perfect agreement, both metrics are zero.

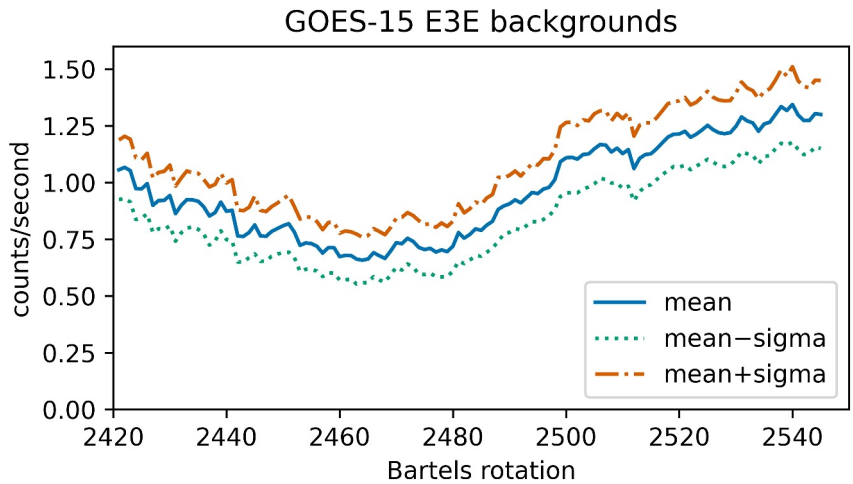

Figure 1. Backgrounds in GOES-15 EPS E3E count rates, January 2011 (BR 2421)–March 2020 (BR 2545). The mean and standard deviation of the Gaussian background distribution are determined for each 27-day Bartels solar rotation (BR). To mitigate jumps in the subtracted background between BRs, the mean backgrounds are interpolated linearly between the midpoints of the BRs, and the interpolated mean backgrounds are subtracted from the E3E count rates.

4. Bowtie Analysis of MPS-HI E10A and E11 Channels as Differential Channels

The response functions of the six MPS-HI channels above 0.6 MeV are shown in Figure 2. For better sampling in the cross-calibration energy range, we have determined the characteristics of E10A and E11 as differential channels using a bowtie analysis similar to that performed on the regularly-processed channels (Boudouridis et al., 2020). The results of the analysis are summarized in Table 1 for channels at 0.55 MeV and above. The results for E6, E7, E8, E9 and E10 and the integral results for E11 were previously reported by Boudouridis et al. (2020). A comparison of the error bars reveals that channels E10A and E11 are better as integral channels than differential channels. However, E11 and E10A as differential channels are similarly accurate to E10, a required differential channel. This result supports the use of E10A and E11, properly characterized, as differential channels. This is possible because realistic electron spectra in this orbit and energy range are quite steep (Boudouridis et al., 2020). This provides two additional differential channels above 1 MeV, a 2.34 MeV channel (from E11) and a 4.43 MeV channel (from E10A).

5. Characterization of EPS E1

5.1. E1 Electron Energy Response Functions

The E1 channel is reported by the D3 dome, one of four major detector subsystems of the EPS (Sellers & Hanser, 1996). The electron response of the E1 channel has been characterized twice, once for the GOES 8–12 series and once for the GOES 13–15 series. The descriptions here of the GOES 8–12 and GOES 13–15 characterizations are taken from Panametrics (1988, 2004), respectively.

On GOES 8–12, the aperture of the EPS D3 dome was covered with an aluminum moderator of areal density 0.123 g cm^{-2}. It was covered by multi-layer insulation (MLI), giving a total aluminum-equivalent density of 0.158 g cm^{-2}. It was calibrated at a linear accelerator producing electron beams with primary energies of 5, 6, 8, 10, and 15 MeV, that were degraded by passage through the accelerator exit window and air to 3.8, 4.8, 6.8, 8.7 and 13.6 MeV. In addition, three separate aluminum absorbers were used to reduce the 5 MeV beam energy to 2.9, 1.8 and 1.1 MeV incident on the instrument. The standard deviation of the beam energies was broadened substantially by scattering in the absorbers to a large fraction of the center energy. From 1.1 to 0.39 MeV, the geometrical factor was determined using a theoretical calculation.

On GOES 13–15, the density of the EPS D3 dome aluminum moderator was the same as on GOES 8–12, but the MLI equivalent density was lower, giving a total density of 0.137 g cm^{-2}. A beam calibration program at a Van de Graaff accelerator was designed to calibrate the response in the lower energy range important for the E1 response that the previous calibration facility could not reach at all or only in a very degraded manner. Accounting for the

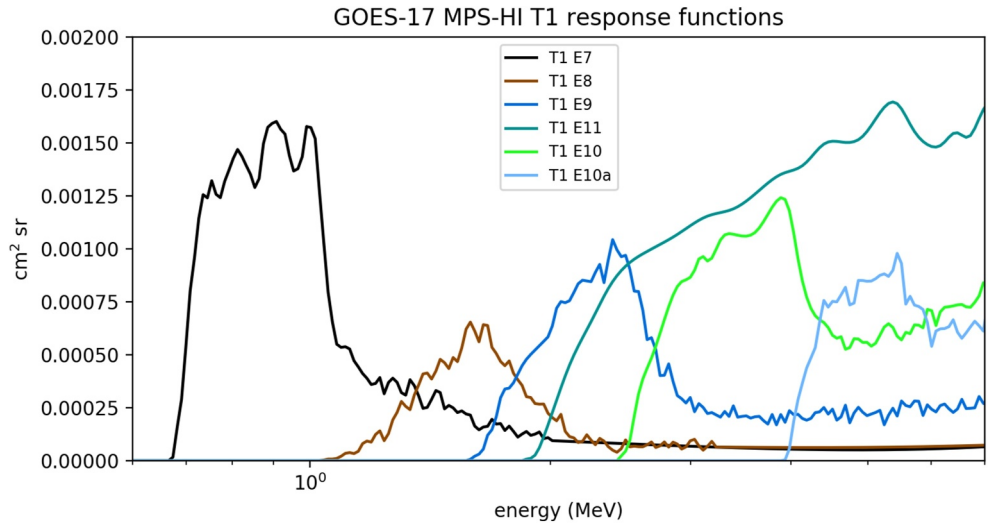

Figure 2. Response functions of the six channels above 0.6 MeV from GOES-17 MPS-HI Telescope 1.

accelerator exit window and air, the energies incident on the instrument were 0.45, 0.57, 0.68, 0.87, 0.96, 1.22, 1.46, 1.89, 2.05, 2.16, and 2.25 MeV.

The results from these two calibrations are plotted together in Figure 3 along with cubic spline fits to subsets of the measured points. All the points from Table 4.8 of Panametrics (1988) and Table 3–18 of Panametrics (2004) are shown. The large variations in the Van de Graaff results above 1 MeV are probably due to experimental error. Therefore, a three-curve family is used to span the range of Panametrics (2004) results above 1 MeV. Although the cubic spline fits do not use all the points, in order to prevent non-physical oscillations, the fits are representative. A fourth cubic spline fit ("NXT-CAL-101") represents the GOES 8–12 results (Panametrics, 1988). The "E1 cubic spline low" curve is essentially the "E1 cubic spline high" curve below 0.9 MeV and the "cubic spline NXT-CAL-101" curve above 0.9 MeV. The four spline fits are used in a sensitivity study in Section 5.3. Below 1 MeV, the theoretical results from the GOES 8–12 characterization are about a factor of 2 greater than the measured results from GOES 13–15, despite the greater equivalent thickness of the MLI for the earlier series. This large discrepancy has a significant effect on the results, as discussed in Sections 5.3 and 5.4.

5.2. Scalar Characterizations of E1

When the processing system changed between the GOES 8–12 and 13–15 series, SWPC updated the EPS E1 characterization to follow the recommendations of Hanser (2011). Thus, the effective lower energy of E1, E_l, was changed to 0.8 MeV and the E1 scalar geometric factor G used in processing increased by a factor of 9.6. These changes did not represent a change in the actual performance of E1, but rather a change in how its gradual response was reduced to a single (energy, geometric factor) pair as if it were a step function. This reassessment

Table 1
Bowtie Analysis Results for GOES-17 MPS-HI Telescope 1 Channels in the 0.55–5 MeV Range

Channel	E_{diff}(MeV)	GdE(cm^2 sr keV)	Error	E_l(MeV)	G(cm^2 sr)	Error
E6	0.547	0.342	−5.8%, +6.7%	–	–	–
E7	0.865	0.554	−6.5%, +9.9%	–	–	–
E8	1.49	0.281	−12.5%, +21.2%	–	–	–
E9	1.97	0.405	−12.1%, +17.2%	–	–	–
E10	2.89	0.647	−1.7%, +32.3%	–	–	–
E10A	4.43	0.634	−3.3%, +35.5%	4.11	0.000705	−0.4%, +3.6%
E11	2.34	0.631	−2.3%, +31.3%	2.07	0.000851	−1.2%, +7.7%

Note. From Boudouridis et al. (2020) and analysis newly reported here.

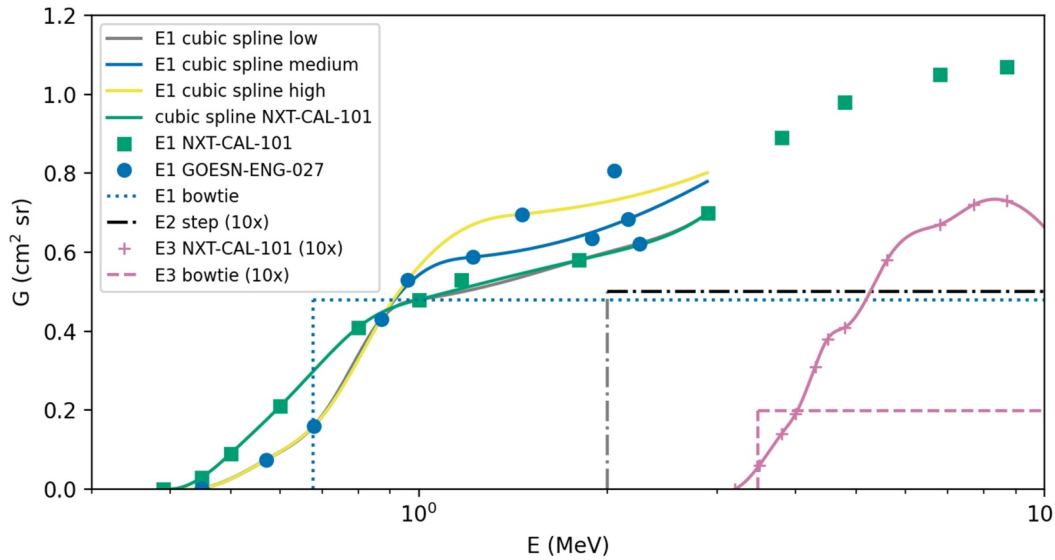

Figure 3. EPS channels E1, E2, and E3 electron response functions used in this paper. The E2 and E3 functions are multiplied by 10. The sources of the data are indicated as follows: NXT-CAL-101 = Panametrics (1988), Tables 4.8 (E1) and 4.10 (E3); GOESN-ENG-027 = Panametrics (2004), Table 3–18.

used the results of a recalibration of the channel (Panametrics, 2004), which had a large effect on the response below 1 MeV (Figure 3). For this paper, the E1 effective (E_l, G) pair has been newly determined using the bowtie analysis approach of Boudouridis et al. (2020), using the same set of electron spectra used to characterize the GOES-16 MPS-HI channels. The E1 response function used in the bowtie analysis is "E1 medium" in Figure 3. The set of effective lower energies and scalar geometric factors for E1 are summarized in Table 2.

5.3. Forward-Model Cross-Calibration of E1 With MPS-HI

The EPS E1 channel almost always reports electron fluxes above backgrounds and is insensitive to MeV solar proton contamination (Rodriguez, 2014b). However, the channel has several problems. Its response function, which turns on and slowly rises from 0.4 to 1.0 MeV (Figure 3), historically has caused problems in interpretation, as discussed in the Introduction. At the highest E1 count rates, the effect of a non-paralyzable dead time (Hanser, 2011) on the D3 Dome detector is large (see Section 5.4). Also, when the E1 fluxes are highly elevated, the E2 fluxes can approach them within a factor of 10, and it has not been possible until now to rule out whether some other instrument non-linearity has been limiting the E1 fluxes under these conditions. Here, we evaluate the performance of the E1 channel over a wide flux dynamic range by performing a comparison of observed E1 count rates with count rates predicted using a forward model. In the forward model, MPS-HI differential spectra are convolved with the E1 response function. The E1 rates have been corrected for dead time, as have the MPS-HI isotropic fluxes run through the forward model.

The observed GOES-15 EPS E1E rates from September 2019 are plotted in Figure 4 along with the forward model predictions using the four spline fits to the E1 response function from Figure 3. (This month is used because the fluxes reached their maximum values in 2019 during this month.) The response function from the GOES 8–12 documentation gives the worst agreement with observations ($\zeta = 129.1\%$). That is, half the prediction errors

Table 2
Effective Lower Energies and Scalar Geometric Factors of EPS Electron Integral Channels E1 and E3 Used Historically in Processing and Derived From Bowtie Analysis for This Paper

	GOES 8–12		GOES 13–15		Bowtie	
Channel	E_l (MeV)	G (cm^2 sr)	E_l (MeV)	G (cm^2 sr)	E_l (MeV)	G (cm^2 sr)
E1	0.6	0.078	0.8	0.75	0.6775	0.4787
E3	4.0	0.0175	4.0	0.056	3.4857	0.0199

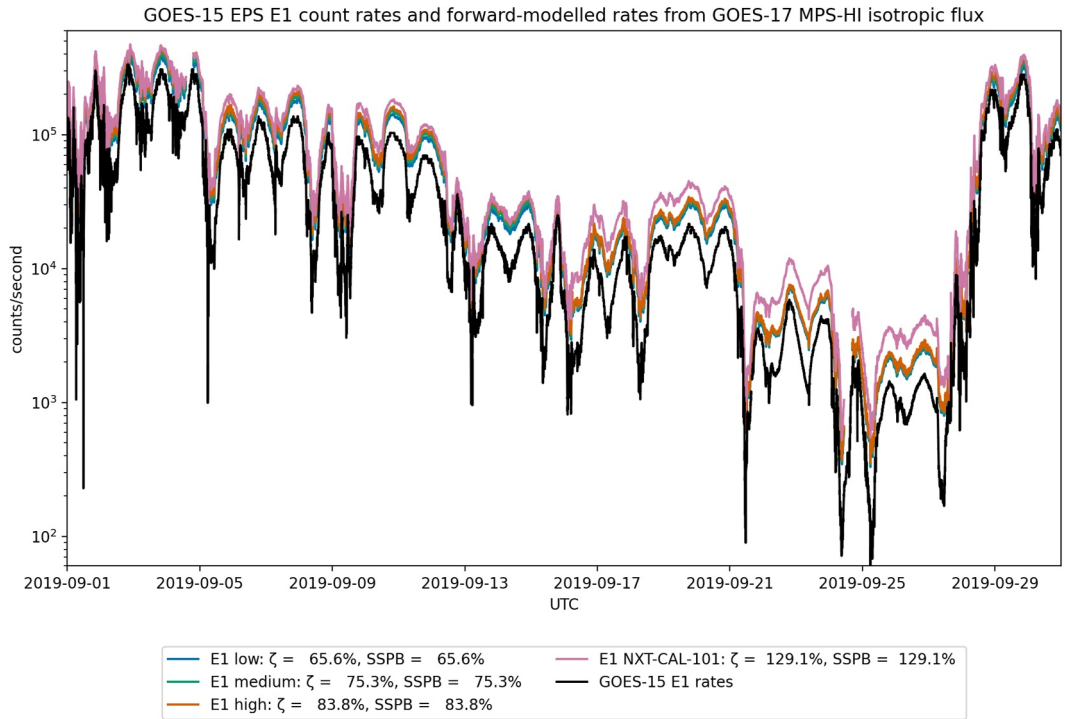

Figure 4. GOES-15 EPS E1E rates (dead-time-corrected) during September 2019, and rates predicted from MPS-HI isotropic-equivalent differential directional flux spectra in a forward-model calculation using the E1 geometric factor functions in Figure 3. The symmetric signed percentage bias (SSPB) and median symmetric accuracy (ζ) of the forward model rates with respect to the observed E1E rates are noted in the legend. The accuracy ratio Q used to calculate these metrics is the ratio of the forward-model-predicted rates to the observed rates.

using the GOES 8–12 response function are greater than a factor of 2.3. Since the GOES 8–12 and the "E1 low" curves ($\zeta = 54.1\%$) are similar above 1 MeV, the difference between these two ζ values indicates the sensitivity to uncertainty in the gradual turn-on of the geometric factor below 1 MeV. Since the GOES 8–12 MLI was thicker, the corresponding response function should be lower, not greater. This result shows that the GOES 8–12 response function was erroneous below 1 MeV. There is also some sensitivity to uncertainty in the geometric factor function above 1 MeV, with the "E1 medium" and "E1 high" curves giving $\zeta = 75.3\%$ and 83.8%, respectively. That is, half the prediction errors using the "E1 medium" response function are greater than a factor of 1.8. In general, the results of Figure 4 show that the E1 response functions or the MPS-HI fluxes are too large, resulting in greater predicted rates than observed. The small spread between the "E1 low," "E1 medium," and "E1 high" forward-model results justifies the decision to use the "E1 medium" response function to derive the E1 bowtie characterization in Section 5.2.

5.4. Accuracy Assessment of E1 Bowtie Results

To assess the accuracy of the three versions of (E_l, G) for E1 (Table 2), we compare observed GOES-15 EPS E1E fluxes to GOES-17 MPS-HI isotropic-equivalent spectra during 2019. The E1E fluxes (processed in real time as >0.8 MeV fluxes) are scaled by the ratios of the geometric factors in Table 2. The MPS-HI spectra are integrated above the effective lower energies in each case. Results for September 2019 are shown in Figure 5. The accuracy metrics ζ and SSPB are calculated treating integrated MPS-HI as the observable and scaled EPS as the prediction. The results in the top panel show that the E1E fluxes calculated using the GOES 8–12 characterization are much greater than the integrated MPS-HI fluxes. The results in the central panel show that the characterization used in real-time GOES 13–15 processing gives better agreement, with the median MPS-HI-derived fluxes now being greater. Both dead-time-corrected and uncorrected E1E fluxes are shown (the real-time processing did not apply a dead-time correction). The Dome D3 dead time is dominated by the E1 count rates and the correction can be quite large (here shown to be about a factor of 2 at peak fluxes). Applying a non-paralyzable dead time correction (Hanser, 2011; Meredith et al., 2015) results in significantly improved ζ and SSPB, resulting from the evident

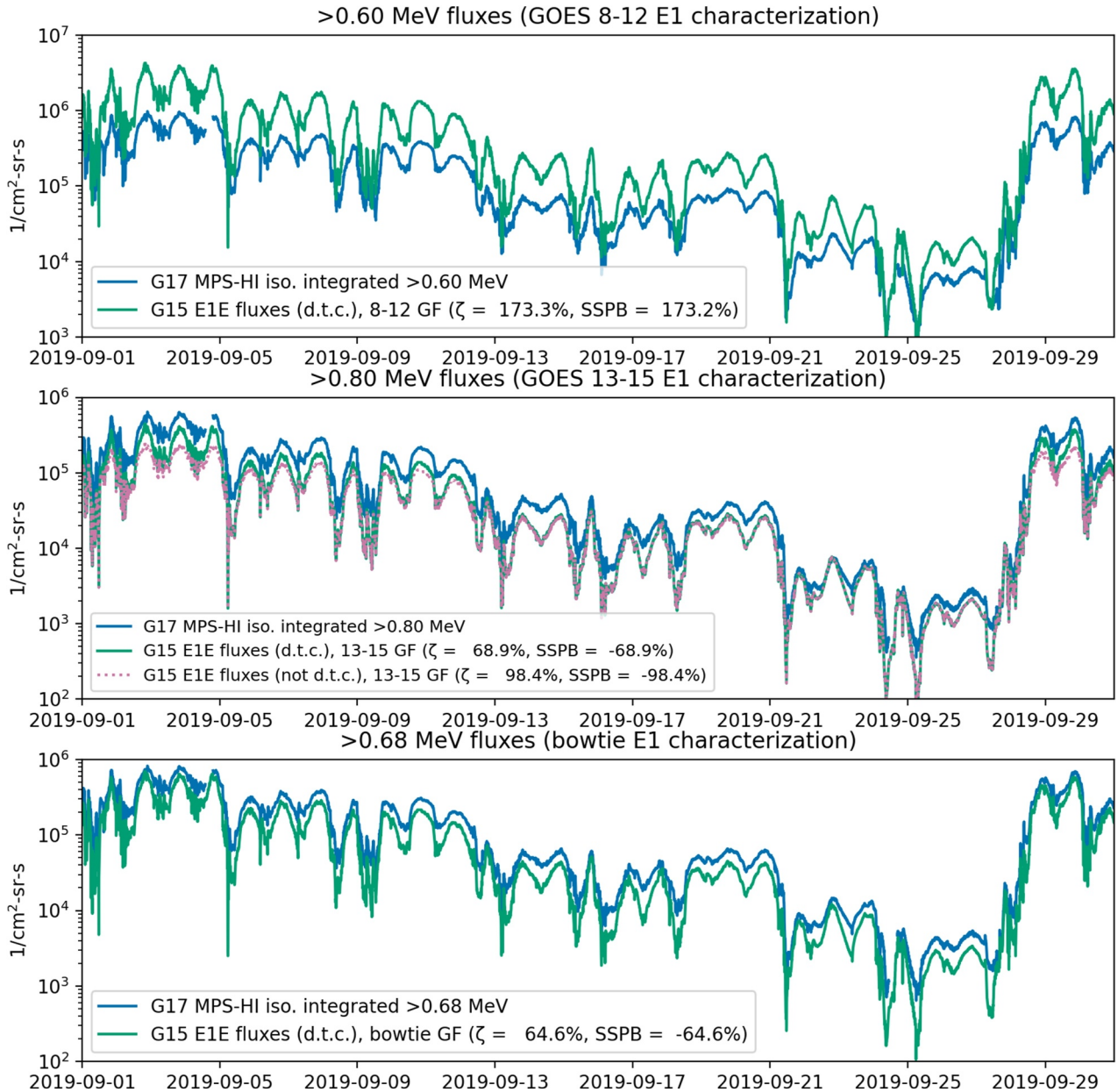

Figure 5. Comparison of isotropic (iso.) averages of GOES-17 MPS-HI differential flux spectra integrated above the indicated energies (blue traces) and GOES-15 E1 count rates converted to integral fluxes using different scalar characterizations of E1 (Table 2) (green traces). In the middle panel, the purple trace represents E1 fluxes that have not been corrected for dead time. The symmetric signed percentage bias (SSPB) and median symmetric accuracy (ζ) of the E1 fluxes with respect to the integrated MPS-HI fluxes are noted in the legends.

improvement in agreement between the GOES-15 and GOES-17 fluxes at the highest levels. The bowtie characterization is in somewhat better agreement with MPS-HI (bottom panel). However, during some months in 2019, the GOES 13–15 characterization gave better agreement with MPS-HI. The range of monthly ζ in 2019 was 50%–74% for the GOES 13–15 characterization and 58%–71% for the bowtie characterization. Although the bowtie characterization has the benefit of less variability in the accuracy, there is not a clear choice in improved accuracy between treating E1 as a >0.68 MeV or as a >0.8 MeV channel. This ambiguity illustrates a key disadvantage of a channel with a slow turn-on. Clearly, however, the old GOES 8–12 characterization was inaccurate, and this justifies scaling the real-time-processed fluxes from that era.

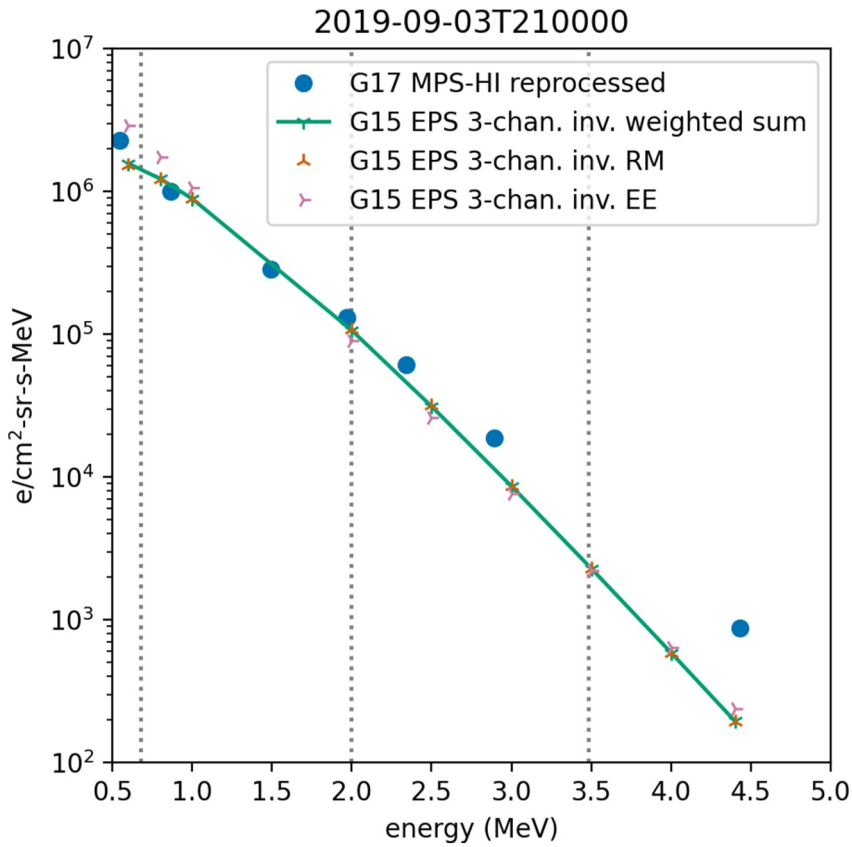

Figure 6. Differential flux spectra from 3 September 2019, 2100 UT, from GOES-15 EPS and GOES-17 MPS-HI observations. The vertical dotted lines indicate the effective lower energies E_l of the EPS integral channels. The GOES-15 spectrum is inverted from the three integral channels E1E, E2E and E3E; the crosses are at the energies reported by the inversion algorithm. The GOES-17 spectrum is as measured by the MPS-HI count rates converted to differential fluxes using the bowtie (E_{diff}, G) scalar pairs in Table 1. As discussed in Section 3.1, RM = relativistic Maxwellian, EE = energy exponential.

6. Characterization of EPS E3

6.1. E3 Electron Energy Response Function

The electron response of the E3 channel has been characterized once, for the GOES 8–12 series (Panametrics, 1988). The aperture of the EPS D4 dome was covered with an aluminum moderator of areal density 1.57 g cm^{-2}. The E3 channel reported all particles depositing 1.53–5.6 MeV in the detector under this moderator (Hanser, 2011). Like E1, it was calibrated using electron beams with primary energies degraded by passage through the accelerator exit window and air to 3.8, 4.8, 6.8, 8.7 and 13.6 MeV (Panametrics, 1988). The other six points in the response function were from a calculation normalized to the results of the beam calibration. The results from this calibration (Table 4.10 of Panametrics (1988)) are plotted in Figure 3.

6.2. Scalar Characterizations of E3

When the processing system changed between the GOES 8–12 and 13–15 series, SWPC updated the EPS E3 characterization to follow the recommendations of Hanser (2011). The E3 scalar geometric factor increased by a factor of 3.2 though its effective lower energy was kept the same. As with E1, this change did not represent a change in the actual performance of E3, but rather a reanalysis of the GOES 8–12 response function. For this paper, the E3 effective (E_l, G) pair has been newly determined using the bowtie analysis approach of Boudouridis et al. (2020), using the same set of electron spectra used to characterize the GOES-16 MPS-HI channels. The set of effective lower energies and scalar geometric factors for E3 are summarized in Table 2. Whether the effective

lower energy is 3.49 or 4.0 MeV, it is clearly sensitive to the shape of the turn-on of the E3 response function. However, there is only one measured point below 4.8 MeV (at 3.8 MeV); the rest are based on the analysis of Panametrics (1988).

6.3. Comparison of EPS E3 With MPS-HI E10A Using Spectral Inversion

When both the EPS E3 and the MPS-HI E10A channels reported fluxes around 4 MeV above backgrounds, MPS-HI reported substantially greater fluxes. A sample comparison is shown in Figure 6 from 3 September 2019, 2100 UT, near local noon when the fluxes are greatest. This day and time are chosen so that any uncertainty in the background correction has an insignificant effect on the comparison. Differential electron flux spectra are inverted from the three EPS integral flux measurements using the method described in Section 3.1. Comparing the shapes of the MPS-HI spectrum and the inverted EPS spectra illustrates how, qualitatively, an energy exponential (EE) spectrum (a straight line on such a plot) or a relativistic Maxwellian (RM) spectrum is a reasonable model for relativistic electron fluxes in GEO, up to 4.4 MeV (Figure 6). Divergence below 1 MeV indicates the need for a second population to fit lower energy fluxes (Denton et al., 2010; Meredith et al., 2023). Between 1 and 3 MeV, the agreement is good. The discrepancy grows from a factor of 2 near 3 MeV to a factor of 5 at 4.4 MeV. The MPS-HI E10A (4.4 MeV) geometric factor is too small (i.e., the fluxes are too large for the observed count rates) or the EPS E3 (>3.49 MeV) geometric factor is too large (i.e., the fluxes are too small for the observed count rates). The E3 response (Figure 3) was partly measured in a beam but not simulated; the MPS-HI E10A response was simulated but not measured in a beam. The simulated response functions of the lower energy MPS-HI channels (from the same telescopes) have been validated and adjusted where possible by beam measurements (Boudouridis et al., 2020). In contrast, EPS E3 is measured by a separate dome detector than E1 and E2, thus any conclusions from their cross-calibrations cannot be applied to E3. For these reasons, the E10A results may be more reliable. However, at the present time, this discrepancy cannot be resolved.

6.4. Accuracy Assessment of EPS E3 Bowtie Results

Because of the observed factor of 2–5 differences between the GOES-15 and the GOES-17 fluxes above 3 MeV (Section 6.3), the E3 (E_l, G) pairs used in the GOES 8–12 and GOES 13–15 processing and from the bowtie analysis are compared differently. Energy-exponential fits to the MPS-HI spectra are integrated above the effective lower energies. The same fits are run through the E3 forward model and converted to fluxes using the scalar G values. Results for September 2019 are shown in Figure 7. The accuracy metrics ζ and SSPB are calculated treating integrated MPS-HI as the observable and the E3 forward model as the prediction. As with E1, the accuracy metrics show that the GOES 8–12 characterization was quite inaccurate, and that the (E_l, G) pair used in the GOES 13–15 real-time processing was a great improvement. The bowtie (E_l, G) pair gives even more accurate results. Note that this is based on a different set of observed spectra than that used in the bowtie analysis. The bowtie (E_l, G) pair is the most accurate scalar representation of the EPS E3 response function to use in quantitative analysis of E3, given our current understanding. These results should be treated with caution. First, this is not an assessment of the absolute accuracy of this response function, which is in question (see Section 6.3). Second, much of the flux range shown in Figure 7 lies below the E3 background level, which is indicated by dotted lines on the panels.

7. Relationship of >0.68 and >2 MeV Electron Fluxes

Good agreement between >2 MeV fluxes from EPS and MPS-HI has been demonstrated via cross-calibrations comparing GOES-13 to -16 and GOES-14 to -16 and -17 (Boudouridis et al., 2020). Starting with GOES-16, SWPC has issued its alerts based on the >2 MeV flux from MPS-HI telescope 4, whose look direction is parallel to the equatorial orbital plane. Since these cross-calibrations were focused on operational continuity, they were performed between EPS and individual MPS-HI telescopes, rather than with an isotropic average calculated from all five MPS-HI telescopes (as in Figures 4 and 5). Since the GOES-15 and -17 >2 MeV fluxes have not been compared before, we repeat this analysis for the study period, prior to assessing the relationship of the E1 and E2 fluxes. We compare the >2 MeV channels from GOES-15 EPS (E2E) and GOES-17 MPS-HI telescopes 1 and 4, the two telescopes whose pitch angles are closest to 90° when the satellite is upright, as it was between 28 March and 8 September 2019. (GOES-17 performed yaw flips twice per year while in operations.) The comparison is performed over the entire dynamic range of the measurements using statistical asynchronous regression (SAR) (O'Brien et al., 2001) (Figure 8). SAR derives a low-noise relationship between two quantities from their

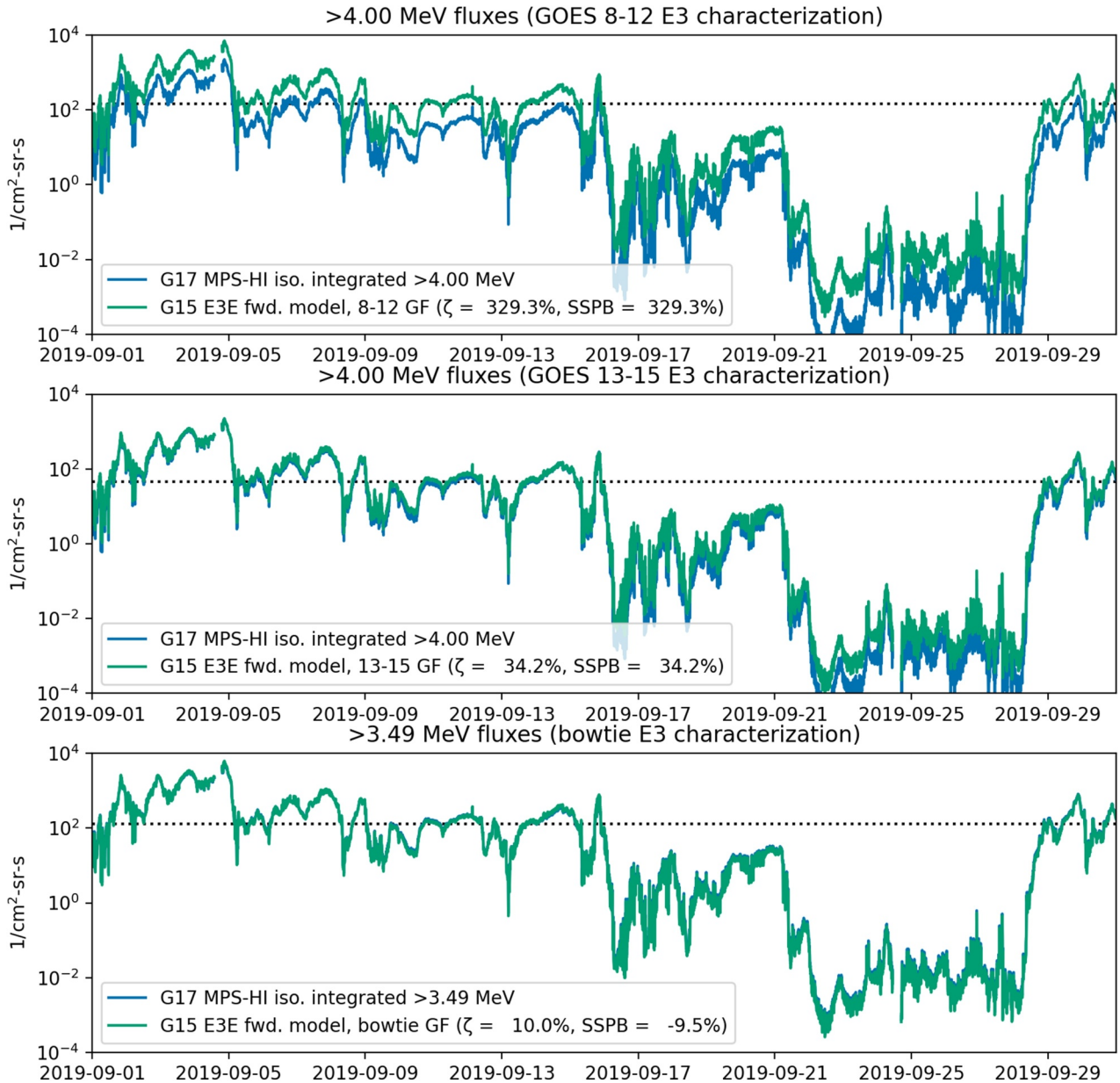

Figure 7. Comparison of two integral flux calculations using extrapolated fits to isotropic (iso.) averages of GOES-17 MPS-HI differential fluxes: flux spectra integrated above the indicated energies (blue traces) and count rate outputs of the EPS E3 forward model converted to integral fluxes using different scalar characterizations of E3 (Table 2) (green traces). In the bottom two panels, the two quantities are sufficiently similar that the blue trace is largely obscured by the green trace. The symmetric signed percentage bias (SSPB) and median symmetric accuracy (ζ) of the forward model with respect to the integrated spectra are noted in the legends. The E3 background level (scaled for different geometric factors) is plotted as a dotted line to indicate the level of backgrounds in the real channel from galactic cosmic rays.

cumulative distribution functions. These regressions confirm the earlier results (Boudouridis et al., 2020) that the EPS >2 MeV fluxes are somewhat greater at the highest levels than the MPS-HI fluxes, though they agree well at the SWPC alert level of 1000 e/cm^2-sr-s. The SAR performed between dead-time-corrected MPS-HI T4 and uncorrected EPS E2E shows better agreement at the highest flux levels. This result raises questions about the dead-time correction applied to EPS E2 and E1 (see Section 8).

The EPS and MPS-HI instruments observe similar >0.68 and >2 MeV integral flux variations over four orders of magnitude. With this new confidence in the magnitude of the EPS integral fluxes at high levels, we evaluate their relationship over a long period (14 months). Figure 9 shows a density plot of the ratio of the GOES-15 >2 and >0.68 MeV fluxes as a function of the >0.68 MeV fluxes for the period January 2019–March 2020. The EPS E1

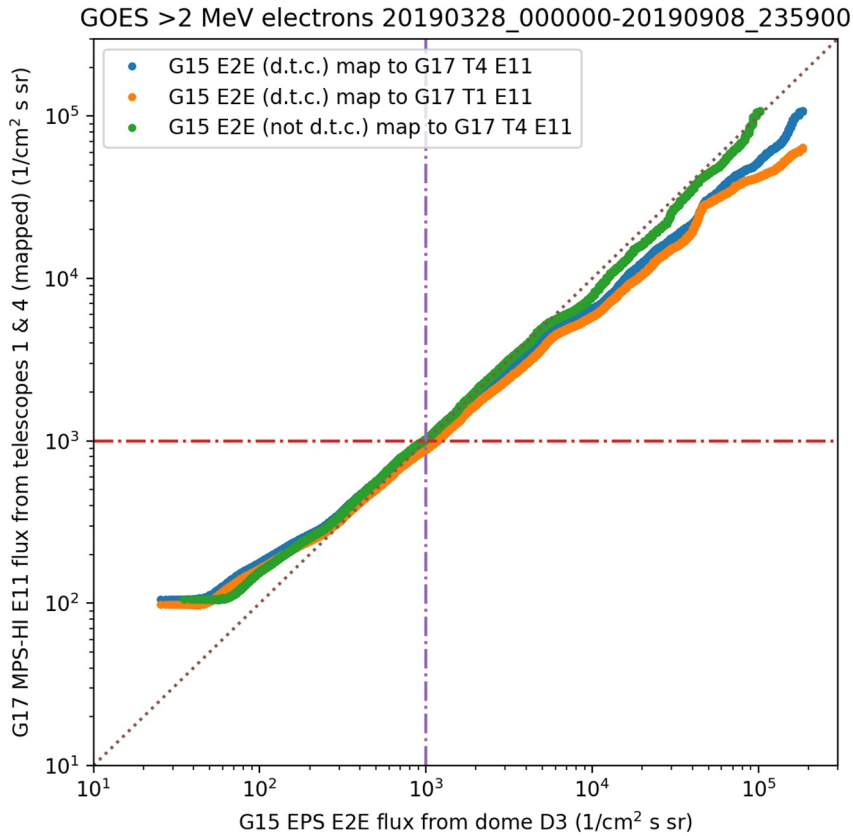

Figure 8. Statistical asynchronous regression between GOES-15 and GOES-17 >2 MeV fluxes over the period 28 March–8 September 2019. The GOES-17 fluxes are from telescopes 1 and 4. The GOES-15 fluxes are from channel E2E. In all three regressions, the MPS-HI fluxes have been corrected for dead time. In one regression (green line), the E2E fluxes have not been corrected for dead time ("not d.t.c.").

channel reported all particles depositing 0.25–1.77 MeV and the E2 channel reported all particles depositing 1.77–10.5 MeV in the Dome D3 detector (Hanser, 2011). Since both channels originate in the same detector, their dead times are the same in the non-paralyzable model and thus have no effect on the ratio. At lower left, the comparison is bounded by the lower level of significance in the >2 MeV fluxes after the background correction, which is determined by a maximum ratio of the background correction to the uncorrected flux of 0.3 (Rodriguez, 2014b). The limit at lower right represents a natural lower limit to the flux ratio that increases more rapidly than the >0.68 MeV fluxes, while the natural upper limit is due to the ratio increasing much more gradually (to a maximum of 0.28). The density plot reveals a broad distribution within these triangular limits. One consequence of this behavior is that the range of spectral temperatures becomes more narrow as the >0.68 MeV flux increases. Another consequence is that, despite clear upper and lower limits to the flux ratio, there is no simple relationship that can be used to predict >2 MeV flux from >0.68 MeV flux. For the use of this data set when an estimate of the differential spectrum is needed, for example, in the calculation of dose or internal charging, there may be little alternative to interpolating the temperature (Denton et al., 2010; Gannon et al., 2012; Onsager et al., 2004) across periods when the >2 MeV flux is below instrument backgrounds.

8. Discussion

In Figures 4, 5, and 7, the similar magnitudes of the symmetric signed percentage bias (SSPB) and median symmetric accuracy (ζ) metrics indicate that systematic offsets dominate random scatter when calculating ζ. These systematic offsets are due primarily to the different (time-invariant) geometric factors used in the analysis. Contributors to both bias and scatter include inaccuracy in the pairing of a geometric factor with a lower energy, an error that depends on the shape of the energy spectrum (e.g., Figure 7, top panel); dead time (Figure 5, middle

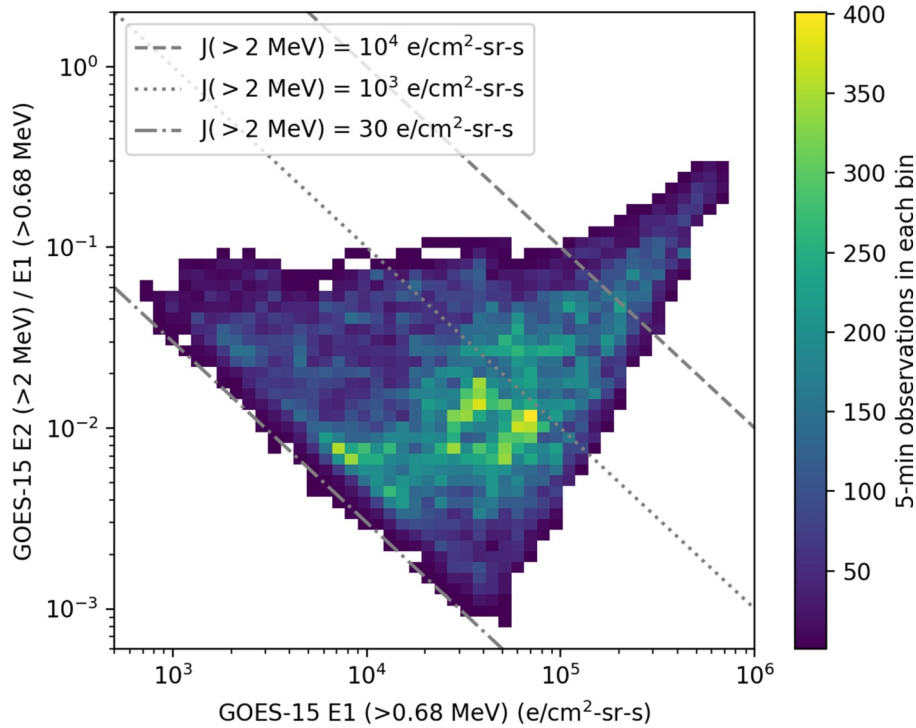

Figure 9. Ratios of GOES-15 >2 and >0.68 MeV dead-time-corrected 5-min-averaged fluxes, 1 January 2019–4 March 2020.

panel), which varies with flux level; and small, fluctuating differences between EPS and MPS-HI fluxes, due to the LT difference, which affect comparisons between forward-model calculations and observed fluxes or rates (Figures 4 and 5). Only when systematic offsets are small is the magnitude of the SSPB significantly different from ζ (Figure 7, bottom panel).

The similar accuracy of the GOES 13–15 (0.8 MeV, 0.75 cm^2 sr) and the bowtie (0.6775 MeV, 0.4787 cm^2 sr) scalar characterizations of the E1 channel highlights an ambiguity of channels that turn on slowly in energy. One possible way to resolve this ambiguity is to compare the correlations of integral fluxes observed by EPS with integral fluxes calculated from MPS-HI differential spectra above the two energies, as in Figure 5. The observed GOES-15 E1E fluxes and the calculated GOES-17 integral fluxes were compared during 2019 for the 0.68 and 0.8 MeV lower energies using logarithms of 5-min averages (Figure 10). The difference between the two cases is that the EPS fluxes are scaled differently and the MPS-HI fluxes are integrated above different energies. The Pearson r^2 values for 0.68 and 0.8 MeV were 0.983 and 0.977, respectively. Both density plots show a sharp peak along the linear fit to the logarithm of the fluxes. The low-level scatter is probably due in part to the 0.6-hr local time difference and to different weighting of the particle energy spectra by the EPS and MPS-HI response functions. While the r^2 value for >0.68 MeV is somewhat greater, the difference is not compelling, and the ambiguity between the two characterizations is not strongly resolved in favor of one characterization or the other. Based on this comparison, it makes sense to continue to treat E1 as a >0.8 MeV channel, given the precedent set by SWPC's use of this characterization for the GOES 13–15 processing and the use of E1 channel data as >0.8 MeV fluxes in recent studies (Baker et al., 2019; Gannon et al., 2012; Glauert et al., 2021). However, if there is need for a >0.68 MeV electron integral flux data set, for example, to help diagnose a spacecraft susceptibility to internal charging by such energies, this analysis shows that the E1 channel count rates can be calibrated accurately as such.

The comparisons in this paper between EPS and MPS-HI give conflicting assessments of the non-paralyzable dead-time correction applied to EPS E2 and E1. In Figure 5 (middle panel), the dead-time correction at the highest flux levels results in more uniform and better agreement between the MPS-HI and EPS E1 fluxes across the entire month. In contrast, in Figure 8, the uncorrected E2 fluxes agree better with the MPS-HI >2 MeV fluxes

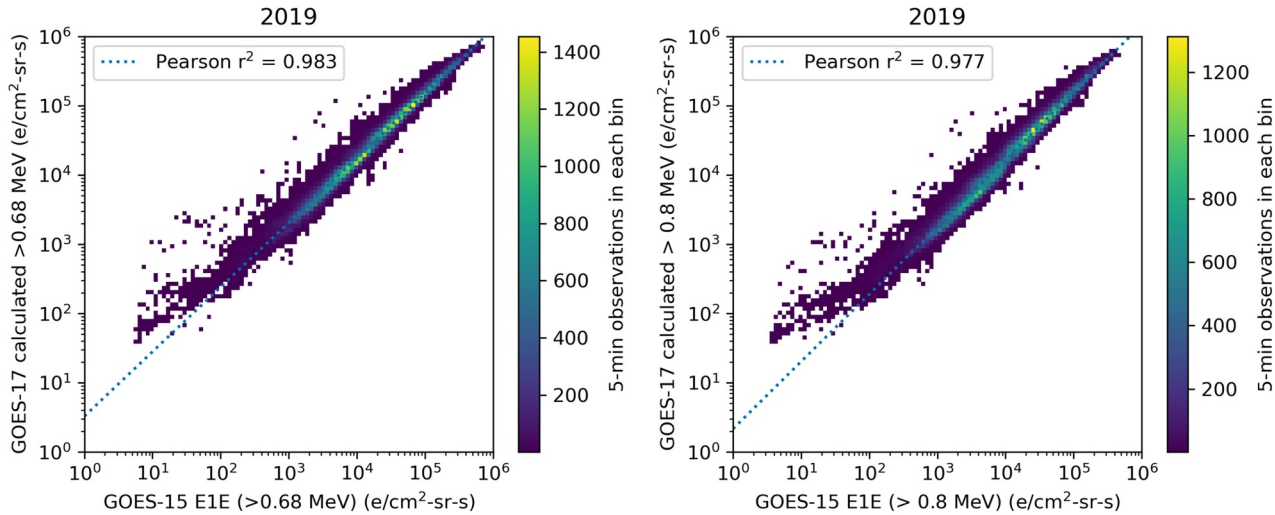

Figure 10. Density plots of integral fluxes calculated from GOES-17 MPS-HI differential fluxes versus integral fluxes observed by GOES-15 EPS E1E during 2019, for a lower energy of 0.68 MeV (left) and 0.8 MeV (right). The integration method is same as that used in Figure 5. There are 103,387 valid points in these comparisons. Linear fits to the logarithms of the fluxes and the Pearson r^2 values from these fits are indicated on the plots.

over the entire dynamic range. (At the low end of the dynamic range, the MPS-HI fluxes approach a limit corresponding to the residual of the background correction.) According to the non-paralyzable model, the proton and alpha channels from the Dome D3 detector should also be affected by the dead time dominated by the E1 rates. However, they do not exhibit evidence of this effect in a superposed epoch analysis of the study period with a period of one day, when the diurnal effect of dead time should be evident in the channel backgrounds in the absence of SEP events. Perhaps the dead time from Hanser (2011) is too large, or the non-paralyzable model is incorrect. This is an ambiguous result that highlights one benefit of a telescope with a small geometric factor and short dead time for measuring extreme fluxes.

The conclusions here about the relative accuracies of the different calibrations of channels E1 and E3 (Table 2) are expected to apply to the entire GOES 8–15 series of EPS flight models. This expectation is based on past cross-comparisons of other channels from the D3 dome (E2, P4) and the D4 dome (P5), which have demonstrated the good repeatability of the EPS design, with differences in the 1%–30% range (Meredith et al., 2015; Rodriguez, 2015; Rodriguez et al., 2014). A 30% difference is smaller than the 69% calibration difference between GOES-15 E1 and GOES-17 (Figure 5), and much smaller than the factor of 2–5 differences between GOES-15 E3 and GOES-17 fluxes (Section 6.3). Nonetheless, the 30% difference observed in past work is large enough to indicate a need for cross-calibration of the GOES 8–15 EPS units prior to the creation of a harmonized time series of E1 and E3 fluxes in the future.

9. Conclusions

The >0.6 and >4 MeV electron fluxes from GOES-15 Energetic Particle Sensor (EPS) have been compared with GOES-17 Magnetospheric Particle Sensor - High Energy (MPS-HI) during 2019, when GOES-15 and GOES-17 were separated by 9.0° (0.6 hr local time) on average, a small separation for two GOES satellites. The symmetric signed percentage bias (SSPB) and median symmetric accuracy (ζ) metrics (Morley et al., 2018) have been used to quantify the comparisons. The absolute magnitude and the shape (determined by the effective energies) of the GOES-17 MPS-HI differential electron flux spectra are being treated as "ground truth" in this analysis. From this comparison, we draw the following conclusions:

1. In general, geometric responses as functions of energy need to be well-characterized and published. This permits improved reassessments of scalar geometric factors, and forward-model analyses or spectral inversions using the full function. In the present work, scalar geometric factors have been reassessed using a bowtie analysis based on a large set of measured spectra (the same method as that used for all GOES MPS-HI instruments) (Boudouridis et al., 2020), and the response functions have been used in forward model and spectral inversion-based comparisons of the two instruments.

2. The (E_l, G) pair used to process GOES 8–12 E1 channels was inaccurate (SSPB and $\zeta = 173\%$). The GOES 13–15 characterization of this channel was more accurate (SSPB = 68.9%, $\zeta = -68.9\%$), after the channel response was measured again below 2.25 MeV and reanalyzed by the instrument contractor. The bowtie characterization is somewhat more accurate (SSPB = 64.6%, $\zeta = -64.6\%$), but the correlation coefficients between the EPS E1 fluxes and the MPS-HI fluxes integrated above the two energies (0.68 and 0.8 MeV) are similar. Since the benefits of applying the E1 bowtie characterization are not compelling, the GOES 13–15 characterization is recommended for continued use, including in correcting the GOES 8–12 E1 calibration (see Appendix A). However, if there is need for a >0.68 MeV electron integral flux data set, the E1 channel data may be scaled accurately as such.
3. The (E_l, G) pair used to process GOES 8–12 E3 channels was inaccurate (SSPB and $\zeta = 329\%$). The GOES 13–15 characterization of this channel, based on reanalysis of the response function by the instrument contractor, was more accurate (SSPB and $\zeta = 34.2\%$). The new E3 bowtie characterization is still more accurate (SSPB = -9.5%, $\zeta = 10\%$) and is recommended for general use, including in correcting the GOES 8–15 calibrations (see Appendix A). These comparisons are based on forward-model calculations using the E3 response function. However, when MPS-HI and EPS fluxes are compared, the EPS fluxes are substantially lower at the highest energies, from a factor of 2 near 3 MeV to a factor of 5 at 4.4 MeV. This discrepancy cannot be resolved at the present time.
4. Cross-calibrations are essential in order to assess the reliability of flux measurements at high fluxes when the accuracy of one instrument is expected to be affected more by non-linearities such as dead time. The cross-calibrations here demonstrate that the EPS E1 and E2 fluxes are reliable, even at the highest count rates. This result makes it possible to conclude with confidence that the E2 >2 MeV flux has a natural lower limit that increases more rapidly than the E1 flux above J(>0.68 MeV) = 5×10^4 e/cm^2-sr-s.
5. Time-varying backgrounds have to be accurately characterized and removed, and insignificant residuals should subsequently be replaced with fill values, so that scientists and models do not confuse these residuals for valid fluxes. The EPS E3 backgrounds are shown to have a solar cycle dependence characteristic of GCRs.
6. At electron energies above 0.6 MeV, owing to the steepness of the electron spectra (approximately energy exponential or relativistic Maxwellian) in GEO, the channel response is dominated by the response function onset, which rises slowly in energy for instruments like EPS with a large field-of-view. This onset must be accurately calibrated and, given limited resources, should be measured at smaller energy and angular intervals than the response at higher energies. For the same reason, two MPS-HI integral channels can be characterized as differential channels with reasonable accuracy, in order to improve the measurement of the spectrum above 2 MeV.
7. The differences between the EPS and MPS-HI electron fluxes have now been quantified over the entire EPS energy range. This permits more accurate interpretation of long-term analyses of space weather effects such as dose damage and internal charging using the ∼25-year time series from the EPS instruments. The differences could be used to cross-calibrate EPS fluxes to MPS-HI prior to analysis, or they could be used as uncertainty estimates in assessing the results of the analyses.

Appendix A: Recommendations for Analysis of Real-Time-Processed EPS Electron Fluxes

Creation of a harmonized GOES 8–15 EPS E1-E3 data set with similar geometrical factors and background corrections remains a project for the future. In the meantime, the following recommendations are made for use of the fluxes that were processed by SWPC in real time and made available retrospectively by NCEI. (On GOES 13–15, the original EPS instrument was renamed EPEAD. The design of the sensor heads was the same, however.)

1. Avoid using E1 and E2 electron fluxes from the GOES-15 EPEAD "W" sensor (`E1W_UNCOR_FLUX`, `E2W_UNCOR_FLUX`, `E1W_COR_FLUX`, `E2W_COR_FLUX`) because of local-time and seasonally-dependent degradation (Baker et al., 2019).
2. Multiply the GOES 8–12 E1 fluxes by 0.104, the ratio of the GOES 8–12 to the GOES 13–15 geometric factors (see Table 2). Associate them with a lower energy of 0.8 MeV.
3. Avoid using the "corrected" E3 fluxes (GOES 8–12: `e3_flux_ic`, GOES 13–15: `E3E_COR_FLUX`, `E3W_COR_FLUX`). Instead, use the "uncorrected" E3 fluxes (GOES 8–12: `e3_flux_i`, GOES 13–15: `E3E_UNCOR_FLUX`, `E3W_UNCOR_FLUX`). The P5 (38–82 MeV) channel from the D4 Dome, like E3, may

be used to identify when a solar proton event is in progress and therefore the data from the E3 channel are dominated by proton fluxes.

4. Multiply the GOES 8–12 uncorrected E3 fluxes by 0.879, and the GOES 13–15 uncorrected E3 fluxes by 2.81, the ratio of their respective geometric factors to the bowtie geometric factor. Associate them with a lower energy of 3.49 MeV.
5. The GOES 8–15 E2 fluxes were processed with the same geometric factor and had the same effective lower energy of 2 MeV. Therefore, scaling of the E2 fluxes is not needed at this time.

Data Availability Statement

The GOES-15 EPS and GOES-17 MPS-HI radiation belt electron fluxes are available from the NOAA National Centers for Environmental Information (NCEI) (NOAA, 2020, 2024c). The GOES-17 magnetometer data are available from NCEI (NOAA, 2024b). GOES-17 Level 0 data are available from the NOAA Comprehensive Large Array-Data Stewardship System (CLASS) (NOAA, 2024a).

Acknowledgments
This research was funded in part through NASA Living With a Star Grant 80NSSC17K0682 to the Space Science Institute, through subaward 01077 to the University of Colorado. It was also funded in part by NOAA cooperative agreements NA17OAR4320101 and NA22OAR4320151. This work was made possible by the efforts of the staff of Panametrics, Inc., including the late F. Hanser, who carefully documented their calibration results, and by the recommendation by T. Onsager (NOAA, retired) that the E1 response function be measured anew for GOES 13–15. We thank Assurance Technology Corporation for making available the MPS-HI response functions. We thank the reviewers for their thoughtful comments on the manuscript, which resulted in important clarifications. The statements, findings, conclusions, and recommendations are those of the authors and do not necessarily reflect the views of NOAA or the U.S. Department of Commerce.

References

Baker, D. N., Zhao, H., Li, X., Kanekal, S. G., Jaynes, A. N., Kress, B. T., et al. (2019). Comparison of Van Allen Probes energetic electron data with corresponding GOES-15 measurements: 2012–2018. *Journal of Geophysical Research: Space Physics*, *124*(12), 9924–9942. https://doi.org/10.1029/2019JA027331

Balikhin, M. A., Rodriguez, J. V., Boynton, R. J., Walker, S. N., Aryan, H., Sibeck, D. G., & Billings, S. A. (2016). Comparative analysis of NOAA REFM and SNB3GEO tools for the forecast of the fluxes of high-energy electrons at GEO. *Space Weather*, *14*(1), 22–31. https://doi.org/10.1002/2015SW001303

Botek, E., Pierrard, V., & Winant, A. (2023). Prediction of radiation belts electron fluxes at a low earth orbit using neural networks with PROBA-V/EPT data. *Space Weather*, *21*(7), e2023SW003466. https://doi.org/10.1029/2023SW003466

Boudouridis, A., Rodriguez, J. V., Kress, B. T., Dichter, B. K., & Onsager, T. G. (2020). Development of a bowtie inversion technique for real-time processing of the GOES-16/-17 SEISS MPS-HI electron channels. *Space Weather*, *18*(4), e2019SW002403. https://doi.org/10.1029/2019SW002403

Chanteur, G., Gendrin, R., & Perraut, S. (1977). Experimental study of high-energy electron drift echoes observed on board ATS 5. *Journal of Geophysical Research (1896-1977)*, *82*(32), 5231–5242. https://doi.org/10.1029/JA082i032p05231

Denton, M. H., Borovsky, J. E., & Cayton, T. E. (2010). A density-temperature description of the outer electron radiation belt during geomagnetic storms. *Journal of Geophysical Research*, *115*(A1). https://doi.org/10.1029/2009JA014183

Dichter, B. K., Galica, G. E., McGarity, J. O., Tsui, S., Golightly, M. J., Lopate, C., & Connell, J. J. (2015). Specification, design, and calibration of the space weather suite of instruments on the NOAA GOES-R program spacecraft. *IEEE Transactions on Nuclear Science*, *62*(6), 2776–2783. https://doi.org/10.1109/TNS.2015.2477997

Fillius, R. W., & McIlwain, C. E. (1974). Measurements of the Jovian radiation belts. *Journal of Geophysical Research*, *79*(25), 3589–3599. https://doi.org/10.1029/JA079i025p03589

Gannon, J., Elkington, S. R., & Onsager, T. G. (2012). Uncovering the nonadiabatic response of geosynchronous electrons to geomagnetic disturbance. *Journal of Geophysical Research*, *117*(A10), A10215. https://doi.org/10.1029/2012JA017543

Glauert, S. A., Horne, R. B., & Kirsch, P. (2021). Evaluation of SaRIF high-energy electron reconstructions and forecasts. *Space Weather*, *19*(12), e2021SW002822. https://doi.org/10.1029/2021SW002822

Grubb, R. N. (1975). *The SMS/GOES space environment monitor subsystem* (Tech. Rep. No. ERL SEL-42). NOAA Space Environment Laboratory. https://www.ngdc.noaa.gov/stp/satellite/goes/doc/ERL-SEL-42_SEM.pdf

Hanser, F. A. (2011). *EPS/HEPAD calibration and data handbook* (Tech. Rep. No. GOESN-ENG-048). Chelmsford, Massachusetts: Assurance Technology Corporation. https://www.ngdc.noaa.gov/stp/satellite/goes/doc/goes_nop/GOESN-ENG-048_RevD_EPS_HEPAD_13May2011.pdf

Lanzerotti, L. J., Roberts, C. S., & Brown, W. L. (1967). Temporal variations in the electron flux at synchronous altitudes. *Journal of Geophysical Research*, *72*(23), 5893–5902. https://doi.org/10.1029/JZ072i023p05893

Lezniak, T. W., Arnoldy, R. L., Parks, G. K., & Winckler, J. R. (1968). Measurement and intensity of energetic electrons at the equator at 6.6 R_e. *Radio Science*, *3*(7), 710–714. https://doi.org/10.1002/rds196837710

Meredith, N. P., Cayton, T. E., Cayton, M. D., & Horne, R. B. (2023). Extreme relativistic electron fluxes in GPS orbit: Analysis of NS41 BDD-IIR data. *Space Weather*, *21*(6), e2023SW003436. https://doi.org/10.1029/2023SW003436

Meredith, N. P., Horne, R. B., Isles, J. D., & Rodriguez, J. V. (2015). Extreme relativistic electron fluxes at geosynchronous orbit: Analysis of GOES E>2 MeV electrons. *Space Weather*, *13*(3), 170–184. https://doi.org/10.1002/2014SW001143

Minow, J. I., Jordanova, V. K., Pitchford, D., Ganushkina, N. Y., Zheng, Y., Delzanno, G., et al. (2024). ISWAT spacecraft surface charging review. *Advances in Space Research*. https://doi.org/10.1016/j.asr.2024.08.058

Morley, S. K., Brito, T. V., & Welling, D. T. (2018). Measures of model performance based on the log accuracy ratio. *Space Weather*, *16*(1), 69–88. https://doi.org/10.1002/2017SW001669

Nelder, J. A., & Mead, R. (1965). A simplex method for function minimization. *The Computer Journal*, *7*(4), 308–313. https://doi.org/10.1093/comjnl/7.4.308

NOAA. (2020). GOES 1-15 space environment monitor particles [Dataset]. *NOAA National Centers for Environmental Information*. https://www.ncei.noaa.gov/data/goes-space-environment-monitor/access/avg/

NOAA. (2024a). Comprehensive large array-data stewardship system [Dataset]. *Author*. https://www.aev.class.noaa.gov/saa/products/welcome

NOAA. (2024b). GOES-R magnetometer (MAG) [Dataset]. *NOAA National Centers for Environmental Information*. https://www.ncei.noaa.gov/products/goes-r-magnetometer

NOAA. (2024c). GOES-R space environment in situ suite (SEISS) [Dataset]. *NOAA National Centers for Environmental Information*. https://www.ncei.noaa.gov/products/goes-r-space-environment-in-situ

O'Brien, T. P., & Morley, S. K. (2011). Documentation of C inversion library (Tech. Rep.). https://github.com/PRBEM/IRBEM-extras/blob/main/invlib/doc/invlib.pdf

O'Brien, T. P., Sornette, D., & McPherron, R. L. (2001). Statistical asynchronous regression: Determining the relationship between two quantities that are not measured simultaneously. *Journal of Geophysical Research*, *106*(A7), 13247–13259. https://doi.org/10.1029/2000JA900193

Oh, D., Kim, J., Loto'aniu, P. T. M., Lim, H., Lee, D., & Kim, D. (2024). Energetic particle flux measurements from the Korean space weather monitor particle detector: A comparative study with the MPS-HI onboard GOES-16. *Earth Planets and Space*, *76*(46), 46. https://doi.org/10.1186/s40623-024-01992-y

Onsager, T. G., Chan, A. A., Fei, Y., Elkington, S. R., Green, J. C., & Singer, H. J. (2004). The radial gradient of relativistic electrons at geosynchronous orbit. *Journal of Geophysical Research*, *109*(A5), A05221. https://doi.org/10.1029/2003JA010368

Onsager, T. G., Grubb, R., Kunches, J., Matheson, L., Speich, D., Zwickl, R. W., & Sauer, H. (1996). Operational uses of the GOES energetic particle detectors. In E. R. Washwell (Ed.), *GOES-8 and beyond* (Vol. 2812, pp. 281–290). SPIE. https://doi.org/10.1117/12.254075

Panametrics. (1988). *GOES I, J, K, L & M EPS dome electron channel calibration report* (Tech. Rep. No. NXT-CAL-101). Panametrics, Inc. Retrieved from https://www.ngdc.noaa.gov/stp/satellite/goes/doc/goes_nop/NXT-CAL-101_EPS_Dome_Electron_16Feb1988.pdf

Panametrics. (1995). *Calibration report for the EPS DOME sensor response to protons* (Tech. Rep. No. NXT-CAL-102). Panametrics Inc. Retrieved from https://www.ngdc.noaa.gov/stp/satellite/goes/doc/goes_nop/NXT-CAL-102_EPS_Dome_Proton_30May1995.pdf

Panametrics. (2004). *Electron Channel calibration report, GOES NO/PQ EPEAD D3 dome* (Tech. Rep. No. GOESN-ENG-027). Waltham. Retrieved from https://www.ngdc.noaa.gov/stp/satellite/goes/doc/goes_nop/GOESN-ENG-027_D3_Electron_23Nov2004.pdf

Paulikas, G. A., & Blake, J. B. (1979). Effects of the solar wind on magnetospheric dynamics: Energetic electrons at the synchronous orbit. In *Quantitative modeling of magnetospheric processes* (pp. 180–202). American Geophysical Union (AGU). https://doi.org/10.1029/GM021p0180

Paulikas, G. A., Blake, J. B., Freden, S. C., & Imamoto, S. S. (1968). Observations of energetic electrons at synchronous altitude: 1. General features and diurnal variations. *Journal of Geophysical Research (1896-1977)*, *73*(15), 4915–4925. https://doi.org/10.1029/JA073i015p04915

Paulikas, G. A., Blake, J. B., & Imamoto, S. S. (1975). ATS-6 energetic particle radiation measurement at synchronous altitude. *IEEE Transactions on Aerospace and Electronic Systems*(6), 1138–1144. https://doi.org/10.1109/TAES.1975.308166

Peck, E. D., Randall, C. E., Green, J. C., Rodriguez, J. V., & Rodger, C. J. (2015). POES MEPED differential flux retrievals and electron channel contamination correction. *Journal of Geophysical Research: Space Physics*, *120*(6), 4596–4612. https://doi.org/10.1002/2014JA020817

Rich, F. J., Califf, S., Loto'aniu, P. T. M., Coakley, M., Krimchansky, A., & Singer, H. J. (2024). Intersatellite comparisons of GOES magnetic field measurements. *Space Weather*, *22*(5), e2023SW003736. https://doi.org/10.1029/2023SW003736

Rodriguez, J. V. (2014a). *GOES 13-15 MAGE/PD pitch angles algorithm theoretical basis document, version 1.0* (Tech. Rep.). NOAA NESDIS National Geophysical Data Center. https://www.ngdc.noaa.gov/stp/satellite/goes/doc/MAGEPD_PitchAngles_Processing_ATBD_v1.0.pdf

Rodriguez, J. V. (2014b). *GOES EPEAD science-quality electron fluxes algorithm theoretical basis document, version 1.0* (Tech. Rep.). NOAA NESDIS National Geophysical Data Center. https://www.ngdc.noaa.gov/stp/satellite/goes/doc/EPEAD_Electron_Science_Reprocessing_ATBD_v1.0.pdf

Rodriguez, J. V. (2015). Cross-calibration of charged particle measurements in geostationary orbit. *GSICS Quarterly Newsletter*, *9*(1), 7–8. https://doi.org/10.7289/V5ZP442R

Rodriguez, J. V., Krosschell, J. C., & Green, J. C. (2014). Intercalibration of GOES 8–15 solar proton detectors. *Space Weather*, *12*(1), 92–109. https://doi.org/10.1002/2013SW000996

Selesnick, R. S., & Blake, J. B. (2000). On the source location of radiation belt relativistic electrons. *Journal of Geophysical Research*, *105*(A2), 2607–2624. https://doi.org/10.1029/1999ja900445

Sellers, F. B., & Hanser, F. A. (1996). Design and calibration of the GOES-8 particle sensors: The EPS and HEPAD. In E. R. Washwell (Ed.), *GOES-8 and beyond* (Vol. 2812, pp. 353–364). SPIE. https://doi.org/10.1117/12.254083

Sillanpää, I., Ganushkina, N. Y., Dubyagin, S., & Rodriguez, J. V. (2017). Electron fluxes at geostationary orbit from GOES MAGED data. *Space Weather*, *15*(12), 1602–1614. https://doi.org/10.1002/2017SW001698

Simms, L. E., Ganushkina, N. Y., Van der Kamp, M., Balikhin, M., & Liemohn, M. W. (2023). Predicting geostationary 40–150 keV electron flux using ARMAX (an autoregressive moving average transfer function), RNN (a recurrent neural network), and logistic regression: A comparison of models. *Space Weather*, *21*(5), e2022SW003263. https://doi.org/10.1029/2022SW003263

Tuszewski, M., Cayton, T. E., Ingraham, J. C., & Kippen, R. M. (2004). Bremsstrahlung effects in energetic particle detectors. *Space Weather*, *2*(10), S10S01. https://doi.org/10.1029/2003SW000057

Vampola, A. L. (1987). Thick dielectric charging on high-altitude spacecraft. *Journal of Electrostatics*, *20*(1), 21–30. https://doi.org/10.1016/0304-3886(87)90083-0

Van Allen, J. A., Baker, D. N., Randall, B. A., & Sentman, D. D. (1974). The magnetosphere of Jupiter as observed with Pioneer 10: 1. Instrument and principal findings. *Journal of Geophysical Research (1896-1977)*, *79*(25), 3559–3577. https://doi.org/10.1029/JA079i025p03559

Wrenn, G. L., Rodgers, D. J., & Ryden, K. A. (2002). A solar cycle of spacecraft anomalies due to internal charging. *Annales Geophysicae*, *20*(7), 953–956. https://doi.org/10.5194/angeo-20-953-2002

Wrenn, G. L., & Smith, R. J. K. (1996). Probability factors governing ESD effects in geosynchronous orbit. *IEEE Transactions on Nuclear Science*, *43*(6), 2783–2789. https://doi.org/10.1109/23.556867